11th International Conference on Fracture Mechanics of Concrete and Concrete Structures
FraMCoS-11
J. M. Chandra Kishen, A. Ramaswamy, S. Ray and R. Vidyasagar (Eds)
https://doi.org/10.21012/FC11.0923102

q-STATISTICAL ANALYSIS OF ACOUSTIC EMISSIONS RECORDED DURING UNCONFINED UNIAXIAL COMPRESSION OF ULTRA HIGH PERFORMANCE CONCRETE

KASHIF NAUKHEZ[1*], R. VIDYA SAGAR[1], J. M. CHANDRA KISHEN[1]

[1]Department of Civil Engineering, Indian Institute of Science, Bangalore 560012, India.

e-mail: [1*]kashifn@iisc.ac.in

Keywords: Acoustic emission, Non-extensive statistical mechanics, Ultra high performance concrete, Inter-event time, Tsallis entropy.

Abstract: This article reports the observations made during the analysis of acoustic emissions (AE) related to the compressive fracture process in ultra high performance concrete (UHPC) in the context of non-extensive statistical mechanics (NESM). The UHPC specimens with different material compositions, namely UHPC-1 (without steel fibres and coarse aggregate), UHPC-2 (with steel fibres and without coarse aggregate), and UHPC-3 (with steel fibres and coarse aggregate) were prepared. The specimens were tested under unconfined uniaxial compression at a loading rate of 0.004 mm/s in the laboratory, and simultaneously the generated AE were recorded. The occurrence of inter-event time (τ) of the successive AE events was used as the fundamental seismic parameter of Tsallis entropy (S_q). The *q*-exponential function for each UHPC specimen follows the complementary cumulative distribution function (CCDF) of τ. The entropic index or *q*-index and the relaxation parameter (β_q) were calculated by fitting the *q*-exponential function to a CCDF-τ plot. The obtained *q*-index and β_q show distinct behaviour in each UHPC specimen. The mixture UHPC-1 shows a continuous decrease in *q*-index reaching a low value of 1.04 near the peak load, resulting in the collapse of the specimen due to the formation of a number of microcracks. On the contrary, a significant increase in *q*-index was observed in UHPC-2 and UHPC-3 after the initial decrease. This may be due to the fibre bridging phenomena and toughening mechanism of coarse aggregate in UHPC-2 and UHPC-3 respectively, which resisted the further crack propagation. The variation in *q*-index of Tsallis entropy provided useful insight about the fracture process using the notion of NESM and therefore, the present study may be useful to understand the compressive fracture mechanism in UHPC.

1 INTRODUCTION

It is known that the fracture process of cementitious materials under mechanical loading is a complex phenomenon [1]. It is important to understand the physical mechanisms behind fracture to prevent the catastrophic failure of structures. To accomplish this, acoustic emissions (AE) were recorded during the quasi-static monotonically increasing mechanical loading. From fracture mechanics perspective, the AE may provide useful insightful information about crack evolution processes, such as nucleation and propagation of microcracks within the material and their mutual interaction to form a network of macrocracks, which ultimately leads to failure of the structure [2]. The AE are transient elastic stress waves generated by the rapid release of stored strain energy when a solid fails due to fracture [3-6]. These waves travel spherically inside the material and are detected by piezoelectric (PZT) sensors mounted on the surface of the test specimen [7].

The fracture process of specimen at the laboratory scale is considered as a model system similar to the rupture phenomena occurred during earthquakes at field scale [8]. The AE recorded during the fracture process under gradually applied mechanical load is

analogous with the release of energy in the earth's crust during seismic events. Therefore, both AE and the earthquake phenomena have similar statistics and exhibits power-law behaviour [9]. Such similarities include, (i) long-range memory effects, (ii) multifractality, and (iii) long-term correlations. These similarities are expressed using the principles of statistical seismology, namely, (i) Omori law, (ii) productivity law, (iii) unified waiting-time scaling law, and (iv) Gutenberg-Richter relationship [11-12]. Consequently, the methods used to study seismic phenomenon may be applied to study fracture process in solids using AE testing [10].

1.1 Non-extensive statistical mechanics

The complex phenomena of fracture at laboratory scale and seismic events at field scale encourages the use of advanced statistical analysis methods. Therefore, non-extensive statistical mechanics (NESM) principles are employed to analyze the complex phenomena in different scales. It is known that NESM was first introduced by Tsallis in 1988 and is a generalization of the Boltzmann-Gibbs equilibrium statistical mechanics [13-14]. NESM, or q-statistics is based on the notion of non-additive Tsallis entropy. It can capture unique features which evolve during fracture process in solids [15].

1.2 Application of NESM to recorded AE

In the present study, NESM is applied to analyze the acoustic emission events recorded during unconfined uniaxial compression of ultra high performance concrete (UHPC) with different material composition. The occurrence of inter-event time (τ) of the successive AE events was used as the fundamental seismic parameter of Tsallis entropy (S_q). The complementary cumulative distribution function (CCDF) of τ was obtained and the entropic index or q-index and the relaxation parameter (β_q) were calculated by fitting the q-exponential function to a CCDF-τ plot.

2 BRIEF LITERATURE REVIEW

Vallianatos and Sammonds applied non-extensive statistical physics (NESP) concept to the earthquake data by analyzing τ and inter-event distance (d) cumulative distributions and the frequency-moment [16]. It was observed that the seismic moment and inter-event time distributions represented a sub-additive system in which the long-range interactions have an important role. Chochlaki et al. studied the Tsallis entropy parameters in Earth's seismic zones for τ and frequency-magnitude distributions under the framework of NESM [17]. Loukidis et al. studied the AE data under uniaxial compression of rock specimens and the τ was analyzed in context of NESM [10]. It was concluded that the deviation from the linear relationship between q and $\frac{1}{\beta_q}$ may act as a pre-failure indicator and can provide insightful information about the damage accumulation in rock specimens. In the study carried out by Loukidis et al. using marble and cement mortar specimens, the τ and d was examined under the NESM concept and it was concluded that NESM is an effective method for detecting the phenomena of criticality [18]. Recently, Vinciguerra et al. studied the rock deformation using Q-statistical analysis using AE in sandstone and granite specimens [19]. The pre-failure processes in both types of rock were characterized using the q-statistics.

Relatively less studies are reported on the fracture process in concrete in context of NESM. The variation of q-index and β_q with the change in material composition are yet to be studied more rigorously. Furthermore, the presence of coarse aggregate and steel fibres in UHPC which causes the toughening mechanism may be explained under the framework of NESM.

The aim was to study the variation of q and β_q until failure of the specimen and correlating this variation with the crack growth mechanisms and compressive fracture processes in UHPC.

3 METHODOLOGY

Tsallis introduced a generalized entropy known as Tsallis entropy (S_q) to describe complex behaviour of a non-equilibrium

stationary states of a system [13,20-21]. Consider a discrete random variable *X* with a probability distribution *p(X)*, then

$$S_q = \frac{k_B}{q-1}\left(1 - \sum_{i=1}^{W}[p_i(X)]^q\right) \quad (1)$$

or if *X* is a continuous random variable,

$$S_q = \frac{k_B}{q-1}\left(1 - \int_0^{\infty}[p(X)]^q\, dX\right) \quad (2)$$

where p_i is the probability of the system being in the i[th] state, k_B is the Boltzmann's constant, q is the entropic index or q-index representing the degree of non-extensivity of the system, W is the total number of microstates present in the system. When q tends to 1, the classical Boltzmann-Gibbs statistical mechanics is recovered and the expression reduces to

$$S_{BG} = -k_B \sum_{i=1}^{W} p_i \ln p_i \quad (3)$$

where S_{BG} is the Boltzmann-Gibbs entropy.
In case with $q > 1$, the system is considered as sub-additive system, satisfying the relation

$$S_q(A+B) < S_q(A) + S_q(B) \quad (4)$$

and for $q < 1$, the system is considered as super-additive system with

$$S_q(A+B) > S_q(A) + S_q(B) \quad (5)$$

Consider two subsystems, A and B, that are statistically independent. The non-additive behaviour of the system is expressed using the Tsallis entropy which satisfies

$$S_q(A+B) = S_q(A) + S_q(B) + \frac{1-q}{k_B} S_q(A)\, S_q(B) \quad (6)$$

where, $S_q(A)$ and $S_q(B)$ is the Tsallis entropy of the subsystem A and B respectively, $S_q(A+B)$ is the Tsallis entropy of the combined subsystem A and B. The last term of the expression represents the non-additivity of the system due to the long-range correlations.

To calculate the probability distribution, $p(X)$ of the random variable *X*, where *X* can be a moment tensor, inter-event time or the inter-event distance between two successive AE events, the non-extensive Tsallis entropy is maximized using the method of Lagrange-multipliers [13]. Hence, the normalization condition of $p(X)$ and the generalized q-expectation, $\langle X_q \rangle$ is used, given by equation (7) and equation (8) respectively.

$$\int_0^{\infty} p(X)dX = 1 \quad (7)$$

$$\langle X_q \rangle = \int_0^{\infty} X P_q(X) dX = 1 \quad (8)$$

where, the escort probability $P_q(X)$ is

$$P_q(X) = \frac{[p(X)]^q}{\int_0^{\infty}[p(X')]^q dX'} \quad (9)$$

The maximization of S_q using equations (7) and (8), leads to the following probability distribution:

$$p(X) = \frac{\left[1-(1-q)\beta_q X\right]^{\frac{1}{1-q}}}{Z_q} \quad (10a)$$

$$p(X) = \frac{exp_q\left(-\beta_q X\right)}{Z_q} \quad (10b)$$

where, Z_q denotes the q partition function and β_q is the entropic quantity related to the Langrange multiplier (β^*), given by equation (10) and (11), respectively.

$$Z_q = \int_0^{X_{max}} \exp_q\left(-\beta_q X\right) dX \quad (11)$$

$$\beta_q = \frac{\beta^*}{c_q + (1-q)\beta X_q} \quad (12)$$

where, the term c_q is defined as:

$$c_q = \int_0^{X_{max}} [p(X)]^q dX \quad (13)$$

The term $\exp_q$ (X) represents the q-exponential function given by:

$$\exp_q(X) = \begin{cases} [1+(1-q)X]^{\frac{1}{1-q}} & \text{for } 1+(1-q)X \geq 0 \\ 0 & \text{for } 1+(1-q)X < 0 \end{cases} \quad (14)$$

The inverse form of equation (14) is known as the q-exponential function

$$\ln_q(X) = \frac{1}{1-q}(X^{1-q} - 1) \qquad (15)$$

When q tends to 1, equations (14) and (15) will correspond to standard exponential and logarithmic function, respectively. When $q > 1$, the q-exponential function shows power-law behaviour with a slope of $-1/(q-1)$, on the contrary, when $0 < q < 1$, the q-exponential function presents a cut-off.

In NESM, the quantity to be compared with the distribution of the observed system is the escort probability distribution, $P_q(X)$ rather than the original probability distribution, $p(X)$ [12,22]. On this basis, the complementary cumulative or decumulative probability distribution of the random variable X is obtained by integrating the probability density function, $p(X)$, and is expressed as the q-exponential function:

$$P(>X) = \int_{X_{min}}^{\infty} P_q(X)dX = exp_q\left(\frac{-X}{X_o}\right) \qquad (16)$$

where,

$$X_o = (1-q)\langle X_q \rangle + \frac{1}{\beta^*} \qquad (17)$$

4 EXPERIMENTAL PROGRAM

4.1 Test specimen

UHPC specimen with different material composition, namely, UHPC-1 (without steel fibres and coarse aggregate), UHPC-2 (with steel fibres and without coarse aggregate), and UHPC-3 (with steel fibres and coarse aggregate) were prepared. All UHPC specimens were cubes having 100 mm side length. Three cubes were tested for each UHPC mixture. The mixture details of the UHPC specimens are given in Table 1.

4.2 Test set up

The specimens were tested under unconfined uniaxial compression at a loading rate of 0.004 mm/s, by following [23]. Four piezoelectric (PZT) sensors of resonant type were mounted using silicon grease as a couplant on the surface of the test specimen to record the generated AE using an eight-channel AE monitoring system. PZT sensors (54 kHz resonant frequency) and preamplifiers with a gain of 40 dB were used to record AE activity.

Table 1: Mixture details of UHPC specimens

Specimen	Mixture details
UHPC-1	CM : FA : SP = 1 : 1.73 : 0.01 W/CM = 0.18 (by weight)
UHPC-2	CM : FA : SF : SP = 1 : 1.73 : 0.14 : 0.015 W/CM = 0.18 (by weight)
UHPC-3	CM : FA : CA : SF : SP = 1 : 0.73 : 0.99 : 0.02 W/CM = 0.18 (by weight)

Note: CM = Cementitious materials (Cement + slag + metakaolin + Micro silica), FA = Fine aggregate, CA = Coarse aggregate, SF = Steel fibres, W = Water, SP = Superplasticizer, W/CM = water to cementitious ratio

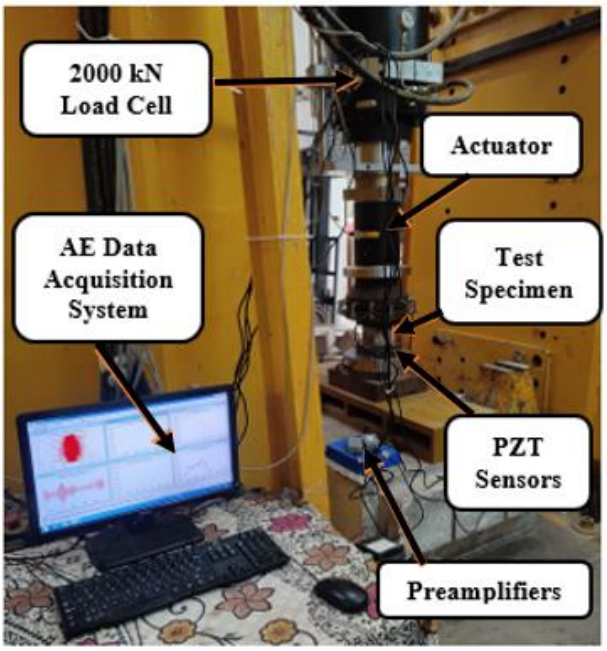

Figure 1: Experimental test set up

The AE detection threshold was set at 40 dB. The timing parameters i.e., PDT (peak definition time), HDT (hit definition time) and HLT (hit lockout time) was set at 200 µs, 800 µs and 1000 µs respectively. The test setup consisted of a servo-controlled hydraulic loading frame of capacity 2000 kN. The specimens were tested in the Structures Laboratory, Department of Civil Engineering, Indian Institute of Science, Bangalore, India.

The test set up is shown in Figure 1.

5 RESULTS AND DISCUSSIONS

In the present study, the notion of NESP was applied to τ, also known as waiting time, defined as the difference of the time interval between two consecutive recorded AE events i.e., $\tau = t_{i+1} - t_i$, where t_{i+1} and t_i is the time of occurrence of $(i+1)^{th}$ and i^{th} AE event, respectively. Therefore, the continuous random variable, X of Tsallis entropy represents the AE parameter of inter-event time, τ.

The AE inter-event time was calculated for different time intervals during the loading stage for each UHPC specimen and complementary cumulative distribution function (CCDF) of τ was obtained. The *q*-index and the relaxation parameter (β_q) were calculated by fitting the *q*-exponential function to a CCDF- τ plot and their variation was observed until the failure of the specimen.

5.1 Total recorded AE events and time of failure for different UHPC specimens

The total number of recorded AE events increases as the material composition changes from UHPC-1 to UHPC-3. Furthermore, the number of AE events recorded before failure was 8781, 11348, and 14102 for UHPC-1, UHPC-2, and UHPC-3, respectively. The time of failure (t_f) recorded at the peak load for mixtures UHPC-1, UHPC-2 and UHPC-3 was 581 s, 967 s and 826 s respectively.

5.2 Recorded AE ring down counts and the variation of AE inter-event time (τ)

The recorded AE ring down counts (RDC) and the variation of moving average of τ is shown in Figure 2, Figure 3 and Figure 4 for UHPC-1, UHPC-2, and UHPC-3, respectively. The variation for RDC and τ is shown in three different subplots with varying time intervals upto failure. A brief explanation of these subplots is given in the subsequent section.

5.3 Estimation of entropic index (*q*) and relaxation parameter (β_q) and their variation

Based on equation (16) and (17), the CCDFs of the AE inter-event times, P (> τ) was obtained and is found to be obey the *q*-exponential function given by:

$$P(>\tau) = exp_q\left(-\frac{\tau}{\tau_q}\right) \qquad (18a)$$

$$\boldsymbol{P}(>\tau) = \left[1 + (1-q)\frac{\tau}{\tau_q}\right]^{\frac{1}{1-q}} \qquad (18b)$$

where, $\tau_q = 1/\beta_q$.

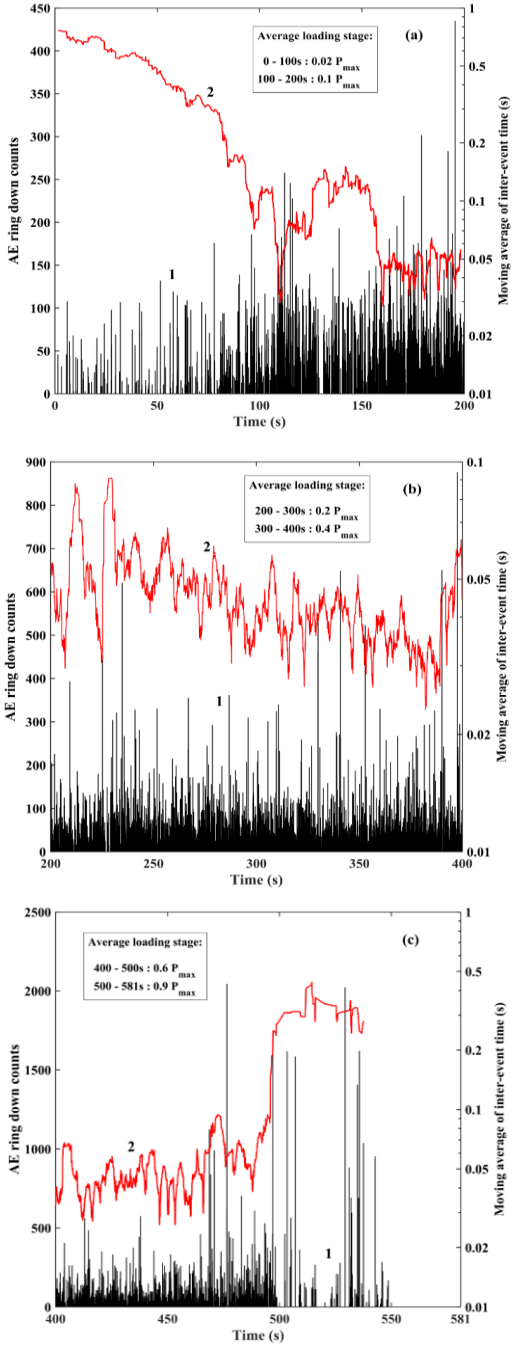

Figure 2: The variation of AE ring down counts and moving average of AE inter-event time for different time durations in UHPC-1.
Note: Notation 1 is AE ring down counts versus time
Notation 2 is moving average of AE inter-event time versus time

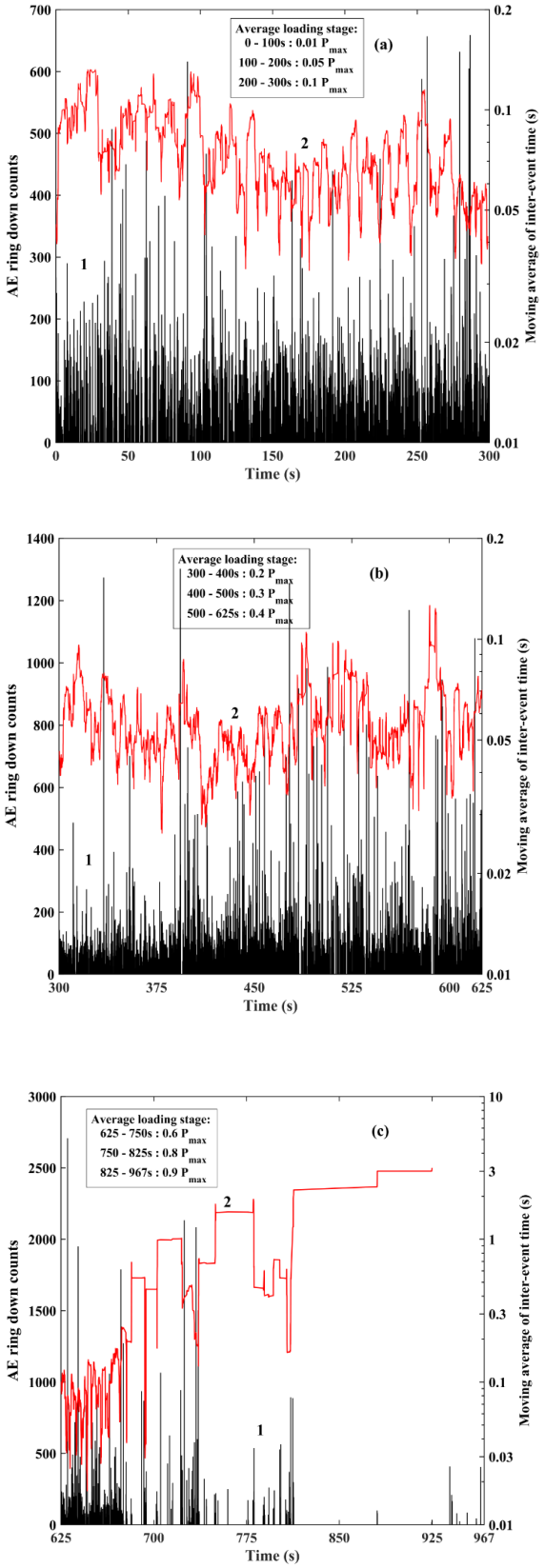

Figure 3: The variation of AE ring down counts and moving average of AE inter-event time for different time durations in UHPC-2

Note: Notation 1 is AE ring down counts versus time
Notation 2 is moving average of AE inter-event time versus time

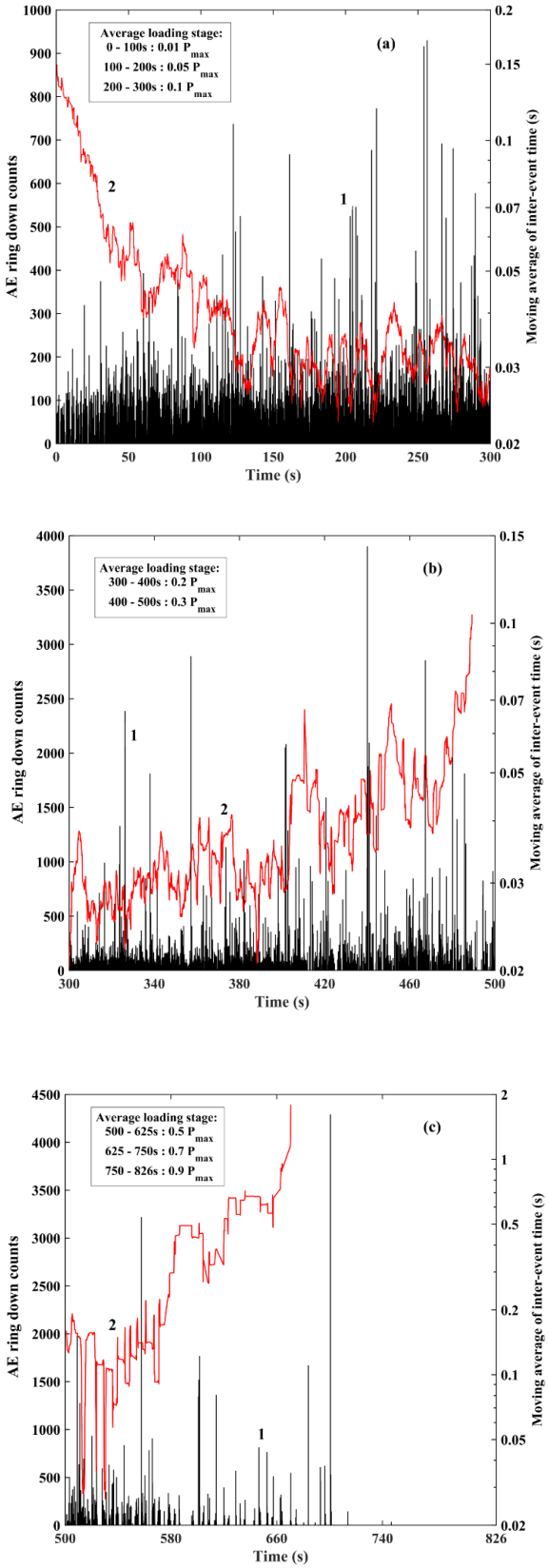

Figure 4: The variation of AE ring down counts and moving average of AE inter-event time for different time durations in UHPC-3

Note: Notation 1 is AE ring down counts versus time
Notation 2 is moving average of AE inter-event time versus time

Table 2: The fitting parameters of the *q*-exponential distribution over different time intervals for UHPC - 1 specimen

Group	Time interval (s)	Entropic index (*q* - index)	Relaxation parameter (β_q)	Average loading stage	Markers
1	0-100	1.8	7.2	0.02 P_{max}	a-a'
2	100-200	1.32	24.4	0.1 P_{max}	b-b'
3	200-300	1.19	26.2	0.2 P_{max}	c-c'
4	300-400	1.16	34.5	0.4 P_{max}	d-d'
5	400-500	1.14	23.3	0.6 P_{max}	e-e'
6	500-581	1.04	3.7	0.9 P_{max}	f-f'

Note: P_{max} indicates the peak load or failure load.

Table 3: The fitting parameters of the *q*-exponential distribution over different time intervals for UHPC - 2 specimen

Group	Time interval (s)	Entropic index (*q* - index)	Relaxation parameter (β_q)	Average loading stage	Markers
1	0-100	1.62	24.2	0.01 P_{max}	a-a'
2	100-200	1.31	22.8	0.05 P_{max}	b-b'
3	200-300	1.28	24.5	0.1 P_{max}	c-c'
4	300-400	1.26	25.7	0.2 P_{max}	d-d'
5	400-500	1.25	31.3	0.3 P_{max}	e-e'
6	500-625	1.24	24.1	0.4 P_{max}	f-f'
7	625-750	1.48	14.1	0.6 P_{max}	g-g'
8	750-825	1.86	12.2	0.8 P_{max}	h-h'
9	825-967	1.56	1.8	0.9 P_{max}	i-i'

Note: P_{max} indicates the peak load or failure load.

Table 4. The fitting parameters of the *q*-exponential distribution over different time intervals for UHPC - 3 specimen

Group	Time interval (s)	Entropic index (*q* - index)	Relaxation parameter (β_q)	Average loading stage	Markers
1	0-100	1.39	29.4	0.01 P_{max}	a-a'
2	100-200	1.25	46.1	0.05 P_{max}	b-b'
3	200-300	1.2	48.5	0.1 P_{max}	c-c'
4	300-400	1.23	43.7	0.2 P_{max}	d-d'
5	400-500	1.43	32.3	0.3 P_{max}	e-e'
6	500-625	1.66	25.9	0.5 P_{max}	f-f'
7	625-750	1.78	5.8	0.7 P_{max}	g-g'
8	750-826	1.47	1.2	0.9 P_{max}	h-h'

Note: P_{max} indicates the peak load or failure load.

The *q*-index and β_q were calculated by fitting the *q*-exponential function to the CCDF-τ plot. The obtained CCDF plot for AE inter-event time and the fitted *q*-exponential function in a log-log representation is shown in Figure 5 for all UHPC specimens. It is observed that the CCDF is fairly described by the *q*-exponential function, following equation (18). However, the precise fittings may not be obtained because of the highly heterogeneous nature of concrete [24]. The obtained values of *q*-index and β_q and the corresponding average loading (P_{avg}) stage, denoted by markers, in different time intervals during loading of the specimen until failure is given in Table 1, Table 2 and Table 3 for UHPC-1, UHPC-2, and UHPC-3, respectively. The markers a, b, c, d, e, f, g, h, i and a', b', c', d', e', f', g', h', i' represents the

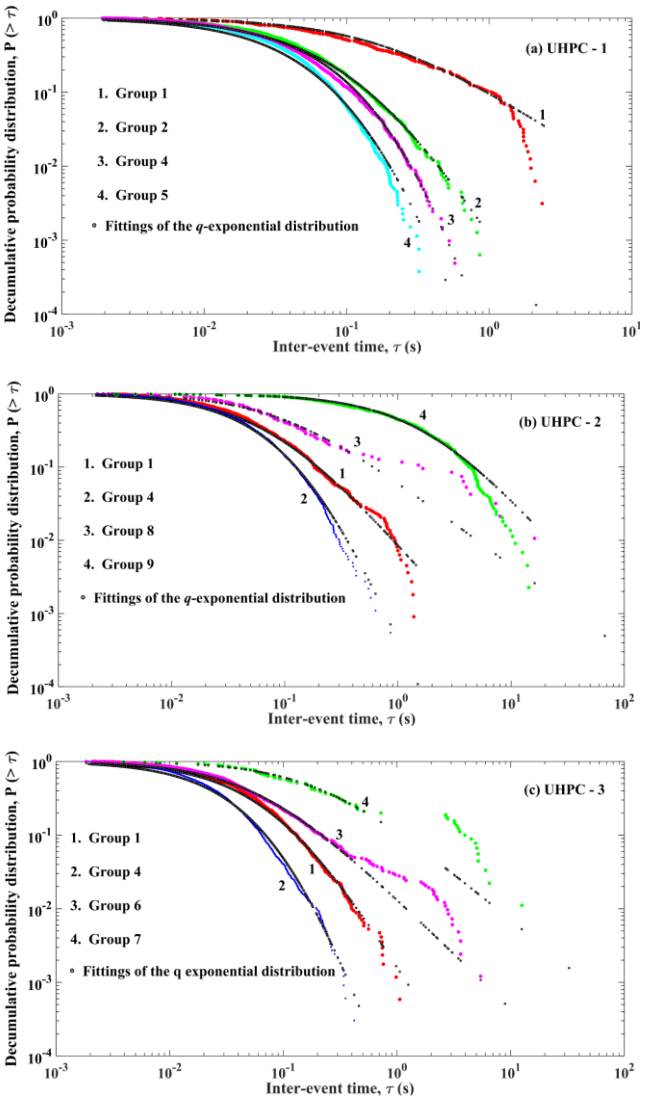

Figure 5: Decumulative probability distribution plot of AE inter-event times, τ (s), and the *q*-exponential fitted curves of different groups for: (a) UHPC-1 (b) UHPC- 2 and (c) UHPC-3 specimens.

various loading stages representing the variation of q and β_q respectively. The variability over different time intervals is shown in Figure 6 for all the UHPC specimens.

5.3.1 Variability of q and β_q

5.3.1.1 UHPC-1

It can be observed from Figure 6a that there is a sudden drop in q-index from 1.8 to 1.32 whereas β_q significantly increases during the first 200s, upto 0.1 P_{max} (point b-b'), where P_{max} is the peak load or failure load. This may be due to crushing of larger pores present in the

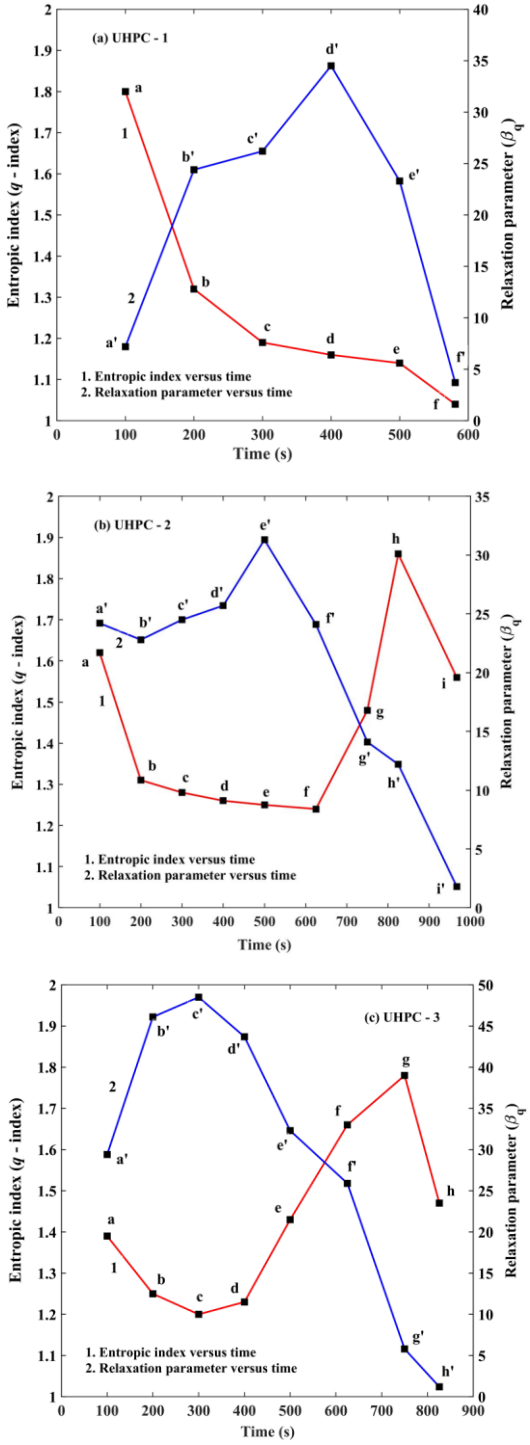

Figure 6: Variation of entropic index (q) and relaxation parameter (β_q) with time for: (a) UHPC- 1 (b) UHPC- 2 and (c) UHPC-3 specimens. The markers a-a' to i-i' on the plots denotes various loading stages for all specimens. Refer table 2, 3 and 4.

concrete and the initiation of cementitious matrix cracking. This can be confirmed from Figure 2a in which the AE activity gradually increases upto 200 s with a simultaneous

decrease in τ. From 200 s to 500 s, the *q*-index gradually decreases to a value of 1.14 as shown in Figure 6a at a loading stage of 0.6 P_{max} (point e). This may be due to the further extension of cracks in the cementitious matrix phase. This is evident from the uniform variation of AE activity and τ as shown in Figure 2b.

The *q*-index further decreases reaching a low value of 1.04 after 500 s with a sharp decrease in β_q near the peak load (0.9 P_{max}) as shown in Figure 6a. This can be attributed to the formation of large number of microcracks on the verge of formation of a macrocrack. This is noticeable in Figure 2c with high values of RDC being recorded with a simultaneous significant increase of τ in vicinity of the peak load. However, afterwards, the specimen failed completely because of the absence of steel fibres and coarse aggregate and hence, no AE activity was recorded.

5.3.1.2 UHPC-2

An instantaneous decrease in *q*-index is observed during the first 200 s from 1.62 to 1.31 as shown in Figure 6b. The decrease may be attributed due to the crushing of large pores and cementitious matrix cracking as observed in UHPC-1. This is evident from the increase in the AE activity and fluctuations during the first 200 s, shown in Figure 3a.

The decrease in *q*-index was gradual from 200 s to 625 s reaching a loading stage of 0.4 P_{max}, whereas an appreciable increase in β_q is observed as shown in Figure 6b (point f-f'). This may be due to extension of cracks in the cementitious matrix phase and the sliding of steel fibres. This is evident from Figure 3b with significant increase in AE activity and large fluctuation in τ.

The *q*-index shows a dramatic increase reaching a high value of 1.86 from 1.24 at 825s at a loading stage of 0.8 Pmax, with a sharp decrease in β_q as shown in Figure 6b (point h- h'). This can be due to the fibre bridging phenomena which delays the further extension of cracks in the cementitious matrix phase. This can be confirmed from Figure 3c with large AE activity being observed in the time interval of 625 s to 800 s. However, afterwards a drop in *q*-index was observed near the peak load (0.9 P_{max}) which may be sliding and debonding of fibres from the cementitious matrix phase, resulting in the failure of specimen. Also, the specimen did not fail completely because of the presence of steel fibres which resisted the further crack propagation, contrary to the case of UHPC- 1. Therefore, the present study may explain the key role of steel fibres in UHPC, in distinction to its role in steel fibre reinforced concrete (SFRC) under uniaxial compression.

5.3.1.3 Variability of *q* and β_q for UHPC-3

A gradual decrease in *q*-index was observed from the initial value of 1.39 with a significant increase in β_q during the first 300 s, attaining a value of 1.2 at a loading stage of 0.1 P_{max} (point c-c'), as shown in Figure 6c. This can be attributed to crushing of pores, cementitious matrix cracking, and cracking in the interfacial transition zone (ITZ) between coarse aggregate and cementitious matrix. This is evident from Figure 4a in which low AE activity is observed with a gradual decrease of τ.

From 300-625 s, a significant increase in *q*-index is observed reaching a value of 1.66 from 1.2, with a gradual decrease in β_q at a loading stage of 0.5 P_{max} (point f), as shown in Figure 6c. It may be due to the toughening mechanism of coarse aggregate i.e., aggregate bridging which delays the further propagation of microcracks as aggregates act as crack arrestors. This can be confirmed from Figure 4b, where very high AE activity are recorded with a gradual increase in τ.

The *q*-index further increases attaining a maximum value of 1.78, however with a lesser rate which may be due to the increased number of microcracks in the ITZ, in the interval of 625-750 s as shown in Figure 6c. This is evident from Figure 4c in which huge spikes of RDC values are observed with a gradual increase in τ. However, a sudden decrease in *q*-index was observed reaching a value of 1.47 with a sharp drop in β_q values, which may be due to the sliding of fibres and debonding of aggregates and fibres from the cementitious matrix near the peak load (0.9 P_{max}) leading to

the failure of the specimen. However, the specimen did not fail completely as in the case of UHPC-1.

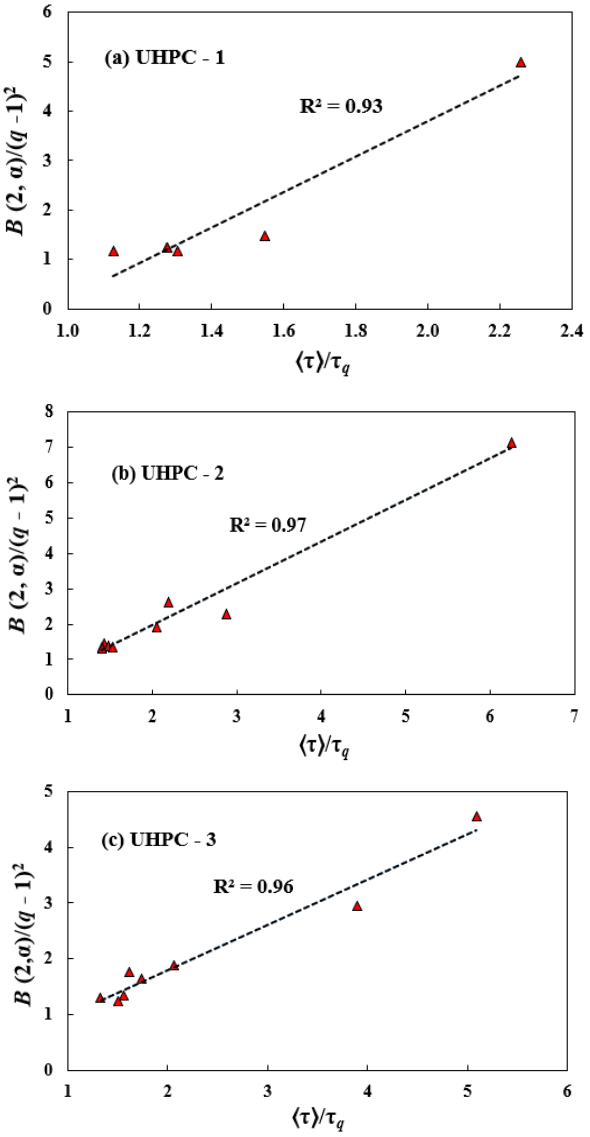

Figure 7: Experimental value, $\langle\tau\rangle/\tau_q$ and predicted value, $B(2, \alpha)/(q-1)^2$ for (a) UHPC-1 (b) UHPC- 2 and (c) UHPC-3

6 COMPARISON OF $\langle\tau\rangle/\tau_q$ AND $B(2, \alpha)/(q-1)^2$ FOR UHPC SPECIMENS

The expectation of AE inter-event time, $\langle\tau\rangle$ is given by the expression:

$$\langle\tau\rangle = \int_{\tau_{min}}^{\tau_{max}} \tau P_q(\tau) d\tau \approx \int_0^{\infty} \tau P_q(\tau) d\tau \quad (19)$$

Substituting, the escort probability distribution from Equation (9) into Equation (19), the following expression is obtained:

$$\frac{\langle\tau\rangle}{\tau_q} = \frac{B\left(2, \frac{2-q}{q-1}\right)}{(q-1)^2} \quad (20)$$

where, $B(2, \alpha)$ refers to the beta function with $\alpha = \frac{2-q}{q-1}$ .The experimental values, $\frac{\langle\tau\rangle}{\tau_q}$ and the predicted values calculated using equation (20) is plotted and is shown in Figure 7. It can be observed that the experimental and predicted values shows good agreement with a coefficient of determination (R^2) of 0.93, 0.97, and 0.96 for UHPC-1, UHPC-2, and UHPC-3 respectively.

7 CONCLUSIONS

The following major conclusions are drawn based on the above experimental observations:

1. The q-exponential function for each UHPC specimen follows the complementary cumulative distribution function (CCDF) of τ.

2. The obtained, q-index and β_q show distinct behaviour in each UHPC mixture composition. The mixture UHPC-1 shows a continuous decrease in q-index reaching a low value of 1.04 near the peak load (0.9 P_{max}) resulting in the collapse of the specimen. This may be due to the further extension of cracks in cementitious matrix phase resulting in the formation of a number of microcracks.

3. On the contrary, in UHPC-2, the q-index decreased to a value of 1.24 which was followed by a significant increase attaining a high value of 1.86 at the loading stage of 0.8 P_{max}. This can be attributed to the fibre bridging phenomena in UHPC-2 which resisted the further crack propagation and hence, the specimen did not fail completely, unlike the case of UHPC-1.

4. Similarly, an appreciable value of 1.78 for q-index was reached in UHPC-3 at the loading stage of 0.7 P_{max} after the gradual decrease to a value of 1.2. It may be due to the toughening mechanism of coarse aggregate which resisted the further propagation of microcracks.

5. The variation in q-index of Tsallis entropy

provided useful insight about the fracture process and also captures the toughening mechanism of steel fibres and coarse aggregate using the notion of NESM. Therefore, the present study may be useful to understand the compressive fracture mechanism in UHPC.

REFERENCES

[1] Thilakarathna, P.S.M., Baduge, K.K., Mendis, P., Vimonsatit, V. and Lee, H., 2020. Mesoscale modelling of concrete–a review of geometry generation, placing algorithms, constitutive relations and applications. *Engineering Fracture Mechanics*, 231, pp.106974.

[2] Sammonds, P.R.; Meredith, P.G.; Main, I.G. Role of pore fluids in the generation of seismic precursors to shear fracture. *Nature* 1992, 359, pp. 228–230.

[3] Ohtsu, M. (1998), Basics of acoustic emission and applications to concrete engineering, *Materials Science Research International*, 4(3), pp. 131-140.

[4] RILEM TC 212-ACD., 2010a. Acoustic emission and related NDE techniques for crack detection and damage evaluation in concrete. Measurement method for acoustic emission signals in concrete. *Materials and Structures*, 43(9), pp. 1177-1181.

[5] RILEM TC 212-ACD., 2010b. Acoustic emission and related NDE techniques for crack detection and damage evaluation in concrete. Test method for damage quantification of reinforced concrete beams by acoustic emission. *Materials and Structures*, 43(9), pp. 1183-1186.

[6] RILEM TC 212-ACD., 2010c. Acoustic emission and related NDE techniques for crack detection and damage evaluation in concrete. Test method for classification of active cracks in concrete structures by acoustic emission. *Materials and Structures*, 43(9), pp. 1187-1189.

[7] Ghadarah, N. and Ayre, D., 2023. A Review on Acoustic Emission Testing for Structural Health Monitoring of Polymer-Based Composites. *Sensors*, 23(15), pp.6945.

[8] Hatton, C.G., Main, I.G. and Meredith, P.G., 1994. Non-universal scaling of fracture length and opening displacement. *Nature*, 367(6459), pp.160-162.

[9] Hanks, T.C., 1992. Small earthquakes, tectonic forces. *Science*, 256(5062), pp.1430-1432.

[10] Abe, S. and Suzuki, N., 2003. Law for the distance between successive earthquakes. *Journal of Geophysical Research: Solid Earth*, 108(B2).

[11] Abe, S. and Suzuki, N., 2005. Scale-free statistics of time interval between successive earthquakes. *Physica A: Statistical Mechanics and its Applications*, 350(2-4), pp.588-596.

[12] Loukidis, A., Stavrakas, I. and Triantis, D., 2023. Non-extensive statistical mechanics in acoustic emissions: Detection of upcoming fracture in rock materials. *Applied Sciences*, 13(5), pp.3249.

[13] Tsallis, C., 1988. Possible generalization of Boltzmann-Gibbs statistics. *Journal of statistical physics*, 52, pp.479-487.

[14] Tsallis, C.; Baldovin, F.; Cerbino, R.; Pierobon, P., 2003. Introduction to Nonextensive Statistical Mechanics and Thermodynamics. In Volume 155: *The Physics of Complex Systems (New Advances and Perspectives)*; IOS Press: Amsterdam, The Netherlands, pp.229–252.

[15] Stavrakas, I.L.I.A.S., Triantis, D.I.M.O.S., Kourkoulis, S.K., Pasiou, E.D. and Dakanali, I.O.A.N.N.A., 2016. Acoustic emission analysis of cement mortar specimens during three point bending tests. *Latin American Journal of Solids and Structures*, 13, pp.2283-2297.

[16] F. Vallianatos, P. Sammonds., 2013. Evidence of non-extensive statistical physics

of the lithospheric instability approaching the 2004 Sumatran-Andaman and 2011 Honshu mega-earthquakes, *Tectonophysics*, 590, pp.52–58.

[17] K. Chochlaki, F. Vallianatos, G. Michas., 2018. Global regionalized seismicity in view of non-extensive statistical physics. *Physica A*, 493, pp.276–285.

[18] Loukidis, A., Triantis, D.; Stavrakas, I., 2020. Non-Extensive Statistical Analysis of Acoustic Emissions Recorded in Marble and Cement Mortar Specimens Under Mechanical Load Until Fracture. *Entropy*, 22, pp.1115.

[19] Vinciguerra, S.C.; Greco, A.; Pluchino, A.; Rapisarda, A.; Tsallis, C., 2023. Acoustic Emissions in Rock Deformation and Failure: New Insights from Q-Statistical Analysis. *Entropy*, 25, pp.701.

[20] C. Tsallis, Nonadditive entropy and nonextensive statistical mechanics- an overview after 20 years. 2009. *Braz. J. Phys*. 39 (2a), pp.337–356.

[21] Saltas, V. & Vallianatos, F. & Triantis, D. & Koumoudeli, T. & Stavrakas, I., 2019. Non-extensive statistical analysis of acoustic emissions series recorded during the uniaxial compression of brittle rocks. *Physica A: Statistical Mechanics and its Applications*, 528, pp.121498.

[22] Abe, S.; Suzuki, N. Law for the distance between successive earthquakes., 2003. *J. Geophys. Res. Solid Earth*,108, pp.2113.

[23] Ronanki, V.S., Aaleti, S. and Valentim, D.B., 2018. Experimental investigation of bond behavior of mild steel reinforcement in UHPC. *Engineering Structures*, 176, pp.707-718.

[24] Greco, A., Tsallis, C., Rapisarda, A., Pluchino, A., Fichera, G. and Contrafatto, L., 2020. Acoustic emissions in compression of building materials: Q-statistics enables the anticipation of the breakdown point, *The European Physical Journal Special Topics*, 229, pp.841-849.